ASTRONOMY & ASTROPHYSICS
SUPPLEMENT SERIES

JULY **1997**, PAGE 85

Astron. Astrophys. Suppl. Ser. **124,** 85-108 (1997)

Further search for OH emission from IRAS sources

V.I. Slysh[1], **A.M. Dzura**[1], **I.E. Val'tts**[1], **and E. Gerard**[2]

[1] Astro Space Center of Lebedev Physical Institute, Profsoyuznaya 84/32, 117810 Moscow, Russia
[2] Departement de Radioastronomie, Observatoire de Paris, Section de Meudon, F-91195 Meudon Principal Cedex, France

Received August 26; accepted October 29, 1996

Abstract. Results of a continued search for OH main line emission from IRAS sources are reported. Towards a sample of 182 sources which consists of IRAS sources selected by the colour criterion for ultracompact HII region, and several IRAS cores, H_2O masers and bipolar outflows, we detected 19 new OH masers of Class I and 5 OH/IR candidates. The correlation between IR and OH maser flux is confirmed. Also 51 thermal and 4 absorption sources were detected. The low radial velocities and derived OH column densities suggest that the thermal OH emission comes from nearby dark clouds. There is evidence that IRAS sources towards which thermal emission was detected are connected with these dark clouds.

Key words: ISM: clouds — ISM: molecules — masers — radio lines: ISM — surveys

1. Introduction

In a previous paper (Slysh et al. 1994, Paper I) we reported results of the extensive search for OH main line emission from a sample of IRAS point sources selected by color criteria from Wood & Churchwell (1989). The sample was restricted to a region outside the galactic plane with galactic latitude $b > 2^\circ$. This search was an extension of the OH masers search towards IRAS sources brighter than 1000 Jy at 60 and 100 μm by Cohen et al. (1988). Several new relatively weak masers were detected as well as thermal OH sources associated with dark clouds. The general conclusion from Paper I was that the detection rate of OH masers from IRAS sources was correlated with their far-infrared flux corroborating a similar conclusion by Moore et al. (1988). The second objective of the search was to detect OH masers less affected by interstellar scattering. This would allow to study maser structures with the high angular resolution of VLBI observations. From pulsar data, it is known that the amount of scattering strongly depends on galactic latitude. For this reason, we selected IRAS sources with galactic latitude $b > 2^\circ$. From pulsar observations, it is also known that the strength of the scattering depends on galactic longitude since the scattering medium is concentrated to the galactic center region. Thus, in the second survey reported in this paper, we also included low latitude IRAS sources in the anticenter region. Also, sources selected for the first survey which had not been observed due to the lack of telescope time, were observed during this second survey. Finally, several IRAS cores from the list of Wood et al. (1994), H_2O masers and bipolar outflows, were added to the observing list.

Send offprint requests to: E. Gerard

2. Observations

The observations were performed in January and March 1994 and in April 1995 with the Nançay radiotelescope. The halfpower beamwidth of the instrument at 18 cm is $3'.5$ in right ascension and $19'$ in declination. The system noise temperature is 45 K at zero declination. The antenna temperatures were converted to flux densities using the efficiency curve of the radiotelescope which is 0.9 K/Jy for point sources at zero declination. An autocorrelation spectrometer consisting of 4 banks of 256 channels with a spectral resolution of 2.25 km s^{-1} was used to observe simultaneously both circular polarizations of the two main OH lines at 1665 and 1667 MHz. The observations were made in the frequency-switching mode with a velocity coverage of 140 km s^{-1}. Sources with known radial velocity in CO line or strong masers were observed with higher velocity resolution. The typical rms noise level after one hour of integration time was about 0.02 to 0.03 Jy.

3. Results

24 new OH masers, 51 thermal emission and 4 absorption sources were detected during the second survey. The new masers are listed in Table 1. Column 1 contains IRAS names, or other names, if there is no associated IRAS source. Column 2 gives the galactic coordinates. Columns 3, 4 and 5 contain Gaussian fit results for the 1667 MHz line, and Cols. 6, 7 and 8 - for the 1665 MHz line. One sigma errors are given in parentheses. Right and left

Table 1. Masers. Column 1 contains IRAS names, or other names. Column 2 – galactic coordinates. Columns 3, 4 and 5 – Gaussian fits for the 1667 MHz line. Columns 6, 7 and 8 – Gaussian fits for the 1665 MHz line. Right and left circular polarizations are designated by R and L, while H and V stand for horizontal and vertical linear polarizations. Capital T is used when a line was supposed to be thermal

Source name	Galactic	1667 MHZ			1665 MHZ		
	coordinates	V, km s^{-1}	FWHM, km s^{-1}	Flux, Jy	V, km s^{-1}	FWHM, km s^{-1}	Flux, Jy
Cas C1	128.5+11.1				16.11(0.04)	0.56(0.41)	0.44(0.07)L
...		3.22(0.11)	1.29(0.47)	0.34(0.06)T	3.43(0.14)	1.11(0.25)	0.27(0.02)T
Cas D1	130.1+11.6	−14.58(0.09)	1.95(0.22)	0.36(0.04)T	−14.86(0.15)	1.81(0.34)	0.24(0.03)T
...					15.19(0.09)	0.56(0.05)	0.38(0.06)L
...					15.00(0.05)	0.56(0.28)	0.35(0.03)R
02460+5929	137.4+0.2			<0.05	−6.49(0.19)	1.12(0.26)	0.16(0.03)L
...					−6.49(0.20)	1.13(0.25)	0.21(0.04)R
03414+3200	160.5−17.8	8.79(0.15)	1.88(0.30)	0.24(0.04)T	−29.26(0.31)	1.23(0.31)	0.20(0.03)L
...					−29.11(0.03)	1.13(0.06)	1.6(0.15)R
05137+3919	168.1+0.8			<0.09	−21.42(0.02)	0.09(0.02)	0.79(0.15)L
...					−21.40(0.04)	0.18(0.01)	2.65(0.12)R
05274+3345	174.2−0.1	−4.55(0.16)	1.71(0.26)	0.23(0.09)L	−3.79(0.08)	1.44(0.31)	0.34(0.11)L
(AFGL5142)		−4.18(0.25)	3.01(0.56)	0.13(0.09)R	−3.39(0.08)	1.54(0.11)	0.68(0.09)R
05379+3550[a]	173.6+2.9	−21.6		<0.5	−21.63(0.03)	0.89(0.07)	0.61(0.04)L
...					−26.83(0.01)	0.59(0.03)	1.57(0.06)R
...					−21.71(0.07)	0.79(0.20)	0.44(0.06)H
...					−26.87(0.02)	0.42(0.05)	0.69(0.07)V
...					−26.8		<0.05L
...					−21.7		<0.05R
05480+2545	183.3−0.6	−3.89(0.03)	0.56(0.20)	0.43(0.03)L	−12.88(0.03)	0.57(0.45)	0.52(0.04)L
...		−4.52(0.24)	0.56(0.30)	0.28(0.02)R	−15.28(0.07)	0.56(0.52)	0.19(0.05)R
...		−9.16(0.27)	2.20(0.60)	0.13(0.03)R	−5.94(0.30)	0.54(0.30)	0.40(0.15)R
...		−18.87(0.31)	2.08(1.34)	0.09(0.03)R	−4.81(0.29)	0.47(0.22)	0.75(0.30)R
06446+0029	212.1−0.7			<0.2	48.65(0.01)	0.25(0.01)	4.76(0.28)L
...					48.96(0.07)	0.43(0.11)	0.83(0.09)L
...					48.64(0.01)	0.26(0.01)	4.90(0.22)R
...					48.96(0.05)	0.36(0.09)	1.00(0.11)R
07111−1211	226.4−0.8	16.54(0.24)	2.93(0.56)	0.12(0.02)L	16.40(0.19)	2.19(0.45)	0.12(0.02)L
...		16.72(0.21)	2.76(0.51)	0.16(0.03)R	16.22(0.07)	1.12(0.20)	0.26(0.05)R
07427−2400	240.3+0.1	63.93(0.02)	0.33(0.05)	0.57(0.07)L	62.94(0.01)	0.23(0.02)	1.62(0.15)L
...		63.96(0.01)	0.06(0.02)	0.41(0.12)R	63.31(0.02)	0.43(0.11)	1.20(0.05)L
...					63.65(0.01)	0.22(0.01)	1.97(0.19)L
...					63.05(0.02)	0.29(0.03)	5.04(0.22)R
...					63.32(0.01)	0.20(0.04)	3.81(0.52)R
...					63.60(0.04)	0.31(0.09)	1.58(0.21)R
...							
...				<0.7H	63.05(0.03)	0.35(0.06)	1.92(0.13)V
...					63.33(0.02)	0.19(0.05)	1.49(0.30)V
...					63.62(0.02)	0.21(0.04)	1.36(0.17)V
...		63.91(0.03)	0.31(0.08)	0.44(0.09)V	63.02(0.02)	0.30(0.04)	2.56(0.23)H
...					63.31(0.02)	0.23(0.06)	2.90(0.36)H
...					63.61(0.03)	0.27(0.06)	2.26(0.22)H
07528−3441[b]	250.6−3.5			<0.02	−26.30(0.01)	0.14(0.09)	0.44(0.05)L
...					−26.30(0.02)	0.14(0.22)	0.30(0.07)R
17269−2235	3.5+6.3	62.50(0.08)	3.11(0.45)	0.60(0.09)	63.50(0.07)	1.50(0.31)	0.9(0.07)[c]
...		99.50(0.11)	2.09(0.23)	2.11(0.10)	98.50(0.13)	1.6(0.17)	0.75(0.09)[c]
17416−2112	6.5+4.2	25.06(0.08)	1.12(0.59)	0.20(0.13)	38.23(0.74)	12.77(1.54)	0.05(0.01)
...		55.76(0.02)	1.26(0.05)	0.69(0.13)			
17576−1845	10.5+2.2	23.58(0.05)	0.83(0.19)	−0.26(0.03)	18.98(0.05)	0.56(0.07)	0.38(0.03)L
17579−3121	359.6−4.1	−10.83(0.14)	2.98(0.36)	0.24(0.03)			<0.07
...		32.90(0.30)	3.92(0.69)	0.13(0.03)			
17589−2312	6.8−0.3	16.74(0.11)	1.60(0.32)	1.27(0.12)L	13.69	0.9	2.13L
...		15.57(0.09)	1.26(0.43)	0.85(0.13)R	15.37	1.07	4.60L
...					16.49	1.07	4.74L
...					16.49	0.9	0.74R
...					21.43	0.79	0.57R
20049+2725	68.8−2.5	6.12(0.45)	3.83(1.09)	0.1(0.02)L	6.28(0.25)	3.27(0.39)	0.19(0.02)L
...		14.54(0.33)	1.13(0.42)	0.12(0.03)L	6.14(0.16)	3.35(0.41)	0.24(0.03)R
...		6.58(0.60)	4.36(1.24)	0.07(0.02)R			
...		14.23(0.12)	1.13(0.20)	0.10(0.02)R			
20144+3526	73.7+0.8	−71.14(0.10)	0.63(0.16)	0.15(0.07)L	−75.62(0.03)	0.64(0.04)	0.58(0.15)L
...		−75.14(0.16)	0.56(0.45)	0.11(0.02)R	−72.36(0.04)	0.63(0.08)	0.55(0.12)L
...		−70.05(0.07)	0.56(0.24)	0.14(0.02)R	−66.93(0.11)	0.81(0.18)	0.20(0.16)L
...					−75.60(0.03)	0.65(0.05)	0.65(0.21)R
...					−68.81(0.12)	0.92(0.31)	0.20(0.21)R
20361+5733	93.9+10.0	−1.60(0.13)	1.28(0.28)	0.13(0.04)L	−1.54(0.13)	1.64(0.38)	0.17(0.01)L
...		14.95(0.26)	1.16(0.58)	0.07(0.04)L	−1.30(0.13)	1.84(0.26)	0.22(0.01)R
...		−1.64(0.19)	1.38(0.41)	0.14(0.05)R			
...		15.07(0.23)	1.23(0.28)	0.12(0.05)R			
20436+5849	95.5+9.9	−2.29(0.04)	0.79(0.06)	0.39(0.03)	−2.36(0.08)	0.88(0.12)	0.24(0.04)
...		3.31(0.10)	0.85(0.17)	0.13(0.01)			< 0.04
21246+5512	96.6+3.4			<0.05	10.49(0.24)	1.20(0.43)	0.11(0.04)L
...					10.35(0.26)	1.13(0.78)	0.12(0.03)R
21432+4719	93.5−4.4	4.01(0.13)	1.61(0.33)	0.13(0.04)	3.69(0.31)	1.47(0.44)	0.08(0.03)
...		21.02(0.36)	1.40(0.23)	0.05(0.02)	19.22(0.23)	1.12(0.09)	0.09(0.02)
22051+5848	103.1+2.7			<0.03	8.46(0.07)	1.13(0.40)	0.13(0.01)L
...					8.50(0.09)	1.13(0.13)	0.08(0.02)R
...		−1.71(0.15)	1.30(0.44)	0.08(0.01)T			

[a] 1665 V profile centered at −21 km s^{-1} and 1665 H profile at −27 km s^{-1}
were not observed with high velocity resolution. [b] Detection reported in the Paper I. [c] These are parameters of 1612 MHz OH line.

Table 2. Thermal sources. Column 1 contains IRAS or other names. Column 2 – associations of an IRAS source with nebulae of Lynds. Column 3 – galactic coordinates. Columns 4, 5, 6 and 7 – results of Gaussian fits. Column 8 contains estimates of OH column density. Column 10 and 11 – CO radial velocities with the corresponding references. Column 11 – name of associated IRAS cloud or core (Wood et al. 1994)

Source Name			Flux, Jy		V	FWHM	N_{OH},	V(CO)	CO	IRAS cloud
IRAS	Lynds	Galactic	1667	1665	km s^{-1}	km s^{-1}	10^{14}cm^{-2}	km s^{-1}	Ref.	or core
03220+3035	1448	157.9−21.5	0.15	0.07	4.1	1.2	2.84			Per A
PerA11	...	157.8−20.7	0.06	0.09	0.9	3.8	1.18			PerA11
			0.10	0.08	7.8	1.2	0.62			
03245+3002	1455	158.8−21.6	0.30	0.13	7.9	2.1	8.97			
03262+3108	1450	158.4−20.5	0.25	0.09	7.8	2.4	9.59	8.4	[1]	Per A2
03439+3233	1471	160.7−17.2	0.12	<0.06	9.9	1.0	2.71			Per A
04016+2610	1491	168.1−19.2	0.13	0.07	7.0	1.3	2.14	7	[2]	Tau K1
04073+3800	1473	160.5−9.8	0.26	0.11	−3.3	1.4	4.54			
04191+1523	...	179.6−23.5	0.15	0.11	6.8	0.9	2.94			
04263+2426	1529	173.4−16.3	0.35	0.19	6.4	1.8	9.61	6.5	[2]	Tau E1
04269+3507	1482	165.4−0.9	0.12	<0.06	−0.2	2.1	3.18	−1	[3]	
04278+2435	1529	173.5−16.0	0.19	0.08	6.2	1.4	4.54	6.2	[4]	
04287+1807	1551	178.7−20.1	0.17	0.08	6.8	1.7	3.06	6.84	[1]	
04325−1419	1642	210.8−36.6	0.19	0.07	0.4	1.3	3.06			
04325+2402	1535	174.7−15.5	0.27	0.10	5.7	1.2	4.55	5.7	[2]	Tau 51
04360+2610	1527	173.5−13.5	0.32	0.27	6.1	1.1	5.34			
04369+2539	1534	174.1−13.7	0.38	0.29	6.2	1.2	8.89	6.82	[1]	Tau A1
05075+3755	...	168.6−1.0	0.09	0.05	−16.6	1.5	1.85		[5]	
05168+3634	...	170.7−0.3	0.06	0.07	−16.2	4.1	2.77	−15	[5]	
05271+3509	...	176.5−1.7	0.16	0.13	−19.5	2.3	4.65	−19.6	[5]	
05283−0412	1640	207.3−19.8	0.22	0.13	11.0	2.3	4.16	10		
RNO 43	...	192.1−11.0	0.14		10.1	0.7	2.03			
05387−0924	1647	213.5−19.9	<0.12	0.18	3.9	2.2	9.28			
05389−0756	1641	212.1−19.2	0.76	0.56	5.0	2.2	30.37			
05435−0015	1627	205.1−14.4	0.21	0.10	10.0	1.6	4.68			Ori A1
05487+0255	1617	203.3−11.9	0.06	0.05	8.5	1.1	0.82			Ori A34
05491+0247	1617	203.5−11.9	0.09	0.05	9.0	2.3	2.56			Ori A2
05496+0812	1598	198.7−9.2	0.08	0.05	11.2	2.2	2.33	13.33	[5]	Ori J
06046−0603	1646	213.3−12.6	0.10	0.05	11.9	3.3	5.03			
06067+2138	...	189.0+1.0	0.16	0.11	2.3	4.0	22.17	3.2	[5]	
06306+0437	...	206.8−1.9	−0.10	−0.09	14.3	5.5		13.97	[5]	
06308+0402	...	207.3−2.2	−0.04	−0.05	0.8	5.5		7.56	[5]	
06343−1036	...	220.8−8.1	0.06	0.04	12.7	4.2	4.46			Mon A
06587−0859	1654	222.1-2.0	0.12	<0.05	40.2	2.4	3.21			
07020−1618	...	229.0−4.6	0.07	0.04	19.5	1.6	1.17	19.58	[5]	
07077−1026	...	224.4−0.7	0.22	0.08	15.5	2.0	5.68	14.1	[5]	
07173−1744	...	231.9−2.1	0.07	<0.06	43.4	2.9	2.36	41.3	[5]	
			0.06	<0.03	48.0	1.2	0.83			
07422−2001	...	236.8+2.0	0.08	0.08	52.3	3.3	1.62	52.7	[5]	
16235−2416	1688	353.1+16.9	0.30	<0.05	3.9	2.3	9.45	3.03	[6]	Oph A1
16242−2422	1688	353.1+16.7	0.64	0.56	3.7	1.6	22.02	3.03		Oph A2
16244−2432	1688	353.0+16.6	0.55	0.38	3.6	1.5	14.53	3.5	[2]	Oph A3
16288−2450	...	353.5+15.6	0.25	0.12	4.2	1.1	3.84	4.35	[7]	Oph A4
16341−1022	...	6.3+23.1	0.07	<0.04	−1.1	0.6				
16442−0930	260;261	8.7+22.2	0.12	0.08	3.7	1.2	1.61	3.4	[1]	
CTB 37 B	...	348.8+0.2	−0.15	−0.12	−7.6	3.2				
			0.12	<0.06	0.8	3.4	5.48			
17130−2053	100	3.1+9.9	0.11	0.07	1.8	1.1	1.70			
18265+0028	570	30.8+5.2	0.22	0.12	8.3	1.8	3.12			
19005−0445	...	30.1−4.7	0.08	<0.05	36.9	4.9	4.62			
20094+2744	824	66.6−3.2	0.14	0.1	5.3	2.9	5.55			
20231+3440	870	74.0−1.7	0.15	0.12	5.8	3.1	6.55			
20568+5217	1003	91.6+4.4	0.22	0.11	−3.5	3.3	10.26	−3	[3]	
21007+4951	...	90.2+2.3	0.14	0.12	−0.8	4.5	6.27	1.1	[5]	
21025+5221	1011	92.3+3.8	0.23	0.16	−1.7	3.0	9.07			
21106+5206	1022	92.9+2.7	−0.48	<0.07	−2.3	2.1				
			−0.2	−0.17	−12.1	2.6				
21161+6141	1125	100.4+8.8	0.12	0.1	0.9	3.5	5.20			
21429+4726	1040	93.5−4.3	0.09	0.07	3.9	0.8	1.48	4	[5]	

[1] Myers et al. (1983), [2] Terebey et al. (1989), [3] Casoli et al. (1986), [4] Heyer et al. (1987),
[5] Wouterloot & Brand (1989), [6] de Geus et al. (1990), [7] Benson et al. (1989).

circular polarizations are designated by capitals R and L, while H and V stand for horizontal and vertical linear polarizations. Capital T is used when a line was supposed to be thermal, and a mean value of fluxes in both circular polarizations is given. When no line was detected, we give upper limits at the velocity position of the line measured in another polarization.

Most of the OH masers detected in this survey belong to type I, i.e. these are masers associated with star-formation regions with strongest emission in the OH main lines at 1665 and 1667 MHz, 1665 MHz being stronger than 1667 MHz.

Five of the masers resemble OH/IR stars: 17269−2235, 17416−2112, 17579−3121, 20361+5733, and 21432+4719 with typical double-peaked spectra at 1667 MHz. Although these sources formally satisfy Wood and Churchwell color criteria for ultracompact HII regions, they are very weak and the errors make their true colors uncertain.

Table 2 contains detections of thermal emission and absorption sources. In Col. 1, IRAS or other names are given, Col. 2 gives the association of an observed IRAS source with dark nebulae from the catalogue of Lynds. Galactic coordinates are listed in Col. 3. Columns 4, 5, 6 and 7 contain the results of Gaussian fits. All sources were observed in both two circular polarizations. Thus, for thermal sources, flux densities were determined from the mean of both polarizations. The LSR velocities and linewidths were determined from the mean of all four spectra (both circular polarizations at 1665 and 1667 MHz).

Column 8 yields the OH molecule column densities towards thermal sources. Since the majority of these sources are very weak (mean flux density $\simeq 0.15$ Jy), and the principal goal of our survey was to detect new OH masers, the integration time for many thermal sources was not sufficient for good line parameter determination. Therefore we did not use parameters of two OH lines at 1665 and 1667 MHz to determine OH column density (as in the method described by Magnani et al. 1988) because the errors on the line ratios were too large. For all detected thermal sources (except 05387−0924) we used 1667 MHz data to determine the OH column density with the following equations (assuming small optical depth):

$$\Delta T_{\rm line} = (T_{\rm ex} - T_{\rm bg})\tau\,,$$

$$\tau = \frac{c^2 A}{8\pi\nu}\frac{g_{\rm u}}{g_{\rm l}}\frac{h\nu}{kT_{\rm ex}}\frac{1.66N_{\rm l}}{\sqrt{\pi}\Delta V}\,,$$

$$N = \frac{N_{\rm l}}{g_{\rm l}} Z \exp\left(\frac{E_{\rm l}}{kT_{\rm rot}}\right)\,,$$

with $\Delta T_{\rm line}$ the observed brightness temperature (obtained by dividing the antenna temperature by the main beam efficiency which equals 0.48 for the Nançay radiotelescope at zero declination, and supposing that thermal sources are broader than the main beam), $T_{\rm ex}$ the excitation temperature, $T_{\rm bg} = 2.7$ K the temperature of the cosmic background radiation, $T_{\rm rot}$ the rotational temperature, A the Einstein value for the transition of frequency ν, $g_{\rm u}$ and $g_{\rm l}$ the statistic weights of the upper and lower levels of a given transition, ΔV the Full Line Width at Half Maximum (FWHM), N and $N_{\rm l}$ the total OH column density and column density of molecules at the lower level and $E_{\rm l}$, the energy of the ground state 18-cm transition.

The statistical sum Z only includes the four lowest hyperfine levels which give rise to OH lines at 18 cm. The energy of the next rotational level with $J = 5/2$ in the $^2\Pi_{3/2}$ ladder is about 85 cm^{-1}. This makes the excitation of this level negligible in the cold clouds towards which we detected thermal OH emission. The excitation temperature $T_{\rm ex}$ and the rotational temperature $T_{\rm rot}$ were arbitrary taken equal to 5 K for all sources. $T_{\rm rot}$ does not cause any serious error because the $E_{\rm l}/kT_{\rm rot}$ ratio is close to zero for any value of $T_{\rm rot}$ within the $5 - 100$ K range. But changing $T_{\rm ex}$ within these boundaries causes a change of $N_{\rm OH}$ by about half an order of magnitude. Thus the values of $N_{\rm OH}$ in Table 2 must be regarded as rough estimates. Finally, Cols. 9 and 10 contain radial velocity of the CO emission with the corresponding references, and Col. 11 – names of a associated IRAS cloud or core from Wood et al. (1994).

4. Comments on individual new masers

The spectra of all detected sources are plotted in Fig. 1 (masers) and Fig. 2 (thermal and absorption sources). Frequency and polarization are marked in the upper right corner of each figure. When no polarization is specified, the spectrum is an average of the right and left hand circular polarizations.

Although we took all precautions to eliminate spurious observations, we cannot exclude the possibility that unnoticed radio frequency interference, in particular from satellites, may have corrupted some spectra.

4.1. Cas C1(128.5+11.1) and Cas D1(130.1+11.6)

These two sources are IRAS cores in IRAS dark clouds identified by Wood et al. (1994). Cas D1 has one association in the IRAS Catalog, but the associated point source is shifted from the position of Cas D1 core by 5′ in right ascension and does not fall in the Nancay radiotelescope main beam. Cas C1 has no any known associated stars or IRAS point sources.

The spectra of Cas C1 and Cas D1 have broad thermal components at $V_{\rm lsr}$ 3 km s^{-1} and −15 km s^{-1} respectively and narrow maser lines at 1665 MHz at 16.11 km s^{-1} for Cas C1 and 15 km s^{-1} for Cas D1. The maser feature in Cas C1 is 100 percent left circular polarized, but the maser in Cas D1 does not exhibit significant circular

polarization. The degree of circular polarization is hereafter defined as the $R-L/R+L$ intensity ratio.

4.2. 02460+5929 (137.4+0.2)

The IRAS source lies in the S198 optical nebula. Blitz et al. (1982) observed the region in the CO $(1-0)$ line and did not have a definite detection. The OH maser at 1665 MHz is unpolarized within errors and has a flux density of 0.2 Jy. At 1667 MHz, we obtained an upper limit of 0.05 Jy.

4.3. 03414+3200 (160.5−17.8)

At 1665 MHz a maser emission was detected with a degree of circular polarization of 78 percent. For our sample the flux density of this maser is rather large – 1.6 Jy. At 1667 MHz we detected a broader thermal line. The velocity of the 1665 MHz maser feature differs from that of the 1667 MHz line by 38 km s^{-1}. This velocity difference probably suggests that the 1665 MHz and 1667 MHz lines come from different objects within the antenna main beam.

4.4. 05137+3919 (168.1+0.8)

We detected a strong (2.7 Jy) maser emission at 1665 MHz with −54 percent circular polarization. Furthermore, the degree of circular polarization varies with velocity and approaches 100 percent in the red wing. At 1667 MHz, an upper limit of 0.09 Jy was obtained. Wouterloot & Brand (1989) observed this source in CO $(1-0)$ line at $V_{\rm lsr}=-25.9$ km s^{-1} which is shifted from the OH maser line by 4.5 km s^{-1}.

4.5. 05274+3345 (170.2−0.1)

A weak narrow maser at 1665 MHz with 33 percent circular polarization was detected towards the infrared source AFGL 5142. Wouterloot & Brand (1989) detected CO emission at −3.9 km s^{-1} coincident with the velocity of the OH maser.

4.6. 05379+3550 (173.6+2.9)

At 1665 MHz, the source emits two circularly polarized features with a velocity difference of 5.2 km s^{-1}. The degree of circular polarization of each feature is greater than 90 percent. Such a profile structure is typical of Zeeman splitting. Supposing that this is a true Zeeman doublet, we derive a value for the magnetic field of 8.8 mgauss which is close to 10 mgauss, the maximum value measured in OH masers. In the 1667 MHz line, the source emits a weak, broad and unpolarized feature at −21.5 km s^{-1}. The IRAS source is situated near the position in the optical nebula S235 observed in the four OH lines at 18 cm by Turner (1979), the separation in right ascension being 5.6 arcminutes. Turner did not detect OH emission. The IRAS source was observed in the H_2O line at 22 GHz by Wouterloot et al. (1988), but no emission was detected.

4.7. 05480+2545 (183.3−0.6)

The 1665 MHz line in the right circular polarization coincides with the strongest 1667 MHz feature at $V_{\rm lsr}=-4$ km s^{-1}. But in the left circular polarization at 1665 MHz, the velocity of the maser feature is −12.9 km s^{-1}, shifted by 8 km s^{-1}. This velocity difference cannot be attributed to Zeeman splitting because the degree of circular polarization is only 18 percent. Wouterloot & Brand (1989) detected CO emission towards this source at −9.6 and 2.6 km s^{-1} radial velocities.

4.8. 06446+0029 (212.1−0.7)

As well as in the previous source, we observe two narrow spectral features in right and left hand circular polarizations at 1665 MHz. But the velocity difference is less than 0.01 km s^{-1}, which gives an upper limit of 0.017 mgauss for the magnetic field. The degree of circular polarization is also small $\simeq 8$ percent. The line profile has a red wing which could be fitted with a Gaussian at a velocity shifted by 0.31 km s^{-1} from the main feature and with an intensity about 6 times smaller. The source was not detected at 1667 MHz. Wouterloot & Brand (1989) detected a CO line towards this source at 44.3 km s^{-1} radial velocity which differs by 5 km s^{-1} from the OH maser line. They also report the presence of wings in the line profile.

4.9. 07111−1211 (226.4−0.8)

The source is rather weak, but the strongest feature in the right circular polarization at 1665 MHz suggests maser excitation. The degree of polarization of the 1665 MHz line is 37 percent. Wouterloot & Brand (1989) detected CO emission at $V_{\rm lsr}=15.24$ km s^{-1}.

4.10. 07427−2400 (240.3+0.1)

This maser was detected by MacLeod (1991) only in the 1665 MHz line. We also detected emission at 1667 MHz with a radial velocity shifted from the 1665 MHz features. We observed with higher velocity resolution and signal-to- noise ratio than MacLeod (1991) and find that the 1665 MHz line consists of three very narrow features shifted in velocity by equal amounts of 0.3 km s^{-1}. The degrees of circular polarization of the 1665 MHz features are respectively 51, 52 and −11 percent. At 1667 MHz, we observed one narrow left-polarized feature shifted by 1.6 km s^{-1} from the center of 1665 MHz line. Wouterloot & Brand (1989) detected CO emission at 67.4 km s^{-1}. The CO line has a red asymmetric top.

4.11. 07528−3441 (250.6−3.5)

The detection of a possible OH maser towards this source was reported in Paper I. We reobserved it at 1665 MHz with higher frequency resolution and confirm the presence of the OH maser with a flux density of 0.4 Jy.

4.12. 17269−2235 (3.5+6.3), 17416−2112 (6.5+4.2), 17579−3121 (359.6−4.1), 20361+5733 (3.9+10.0) and 21432+4719 (93.5−4.4)

These sources resemble OH/IR stars with their typical double peaked spectra at 1667 MHz. 17269−2235 was also observed at 1612 MHz with the same OH/IR line profile as at 1667 MHz. 17416−2112 has a weak broad line at 1665 MHz in the velocity range extending between the two narrow 1667 MHz components. 17579−3121 was not detected at 1665 MHz. However, both 20361+5733 and 21432+4719 show a double-peaked pattern at 1665 MHz. Towards 21432+4719, Wouterloot & Brand (1989) detected CO line emission at 4.80 km s^{-1}.

4.13. 17576−1845 (10.5+2.2)

At 1665 MHz, this source emits a 100 percent circularly polarized line at $V_{\rm lsr} = 19$ km s^{-1}. At 1667 MHz we detected a broad absorption feature, possibly from a cloud in which the 1665 MHz maser is embedded.

4.14. 17589−2312 (6.8−0.3)

This OH maser near W28 was discovered by Gaylard et al. (1994). The maser features are superimposed on a strong broad absorption. The maximum flux density at 1665 MHz is 4.7 Jy. The degree of left circular polarization of the strongest feature at 1665 MHz is close to 100 percent.

4.15. 20049+2725 (68.8−2.5)

The source contains a broad maser (flux density at 1665 MHz greater than at 1667 MHz) unpolarized line at $V_{\rm lsr} = 6$ km s^{-1}. But at 1667 MHz, a narrow feature is also present at 14 km s^{-1}. The spectra resemble 20361+5733 where, along with a broad unpolarized maser feature at −1.5 km s^{-1}, we detected a narrow and weak line at 1665 MHz at $V_{\rm lsr} = 14$ km s^{-1}.

4.16. 20144+3526 (73.7+0.8)

The source exhibits three maser features at 1665 MHz with radial velocities of −76, −72 and −68 km s^{-1}. The first and third features are unpolarized within errors, while the second one has almost 100 percent left circular polarization. At 1667 MHz, the maximum flux density is about 0.15 Jy which is more than 3 times weaker than the 1665 MHz emission.

4.17. 20436+5849 (95.5+9.9)

The source has a two-peaked line profile at 1667 MHz with a velocity difference of 5 km s^{-1}. The flux ratio of the peaks is 3. At 1665 MHz, only the strongest feature is seen, so the ratio must be greater than 6.

4.18. 21246+5512 (96.6+3.4)

Towards this source, a weak unpolarized emission was detected at 1665 MHz. At 1667 MHz, an upper limit of 0.05 Jy was set. Wouterloot & Brand (1989) detected towards this source CO emission at $V_{\rm lsr} = -62.39$ km s^{-1}. The CO velocity differs from that of OH by 73 km s^{-1}, the $V_{\rm lsr}$ of OH maser being 10 km s^{-1}. The features are thus different objects in the antenna main beam.

4.19. 22051+5848 (103.1+2.7)

At 1665 MHz, we detected towards this source a weak unpolarized emission at 8.5 km s^{-1}. The emission at 1667 MHz is shifted by −10 km s^{-1} and its radial velocity coincides with the CO line detected at $V_{\rm lsr} = -1.75$ km s^{-1} by Wouterloot & Brand (1989).

5. Discussion

We observed a total of 182 sources. We found 24 certain and 5 possible OH masers. This represents a 12.6 percent detection rate. This value rises to 15.4 if the 5 possible OH masers are included. For all detected masers, the ratio $F_{\rm OH}(1665)/F_{\rm IR}(60\ \mu{\rm m})$ is always less than 2.5 percent which confirms the conclusion of Cohen et al. (1988) that IR pumping of OH masers is plausible. The correlation of OH at 1665 MHz and infrared flux at 60 μm is shown in Fig. 3. All masers but one fall below the line $F_{\rm OH} = 0.024\ F_{\rm IR}$. In this survey we did not detect any unquestionable masers of Ib type with dominant emission at 1667 MHz (the definition of Ib type is given in Paper I). However four weak possible candidates were detected. Also five possible OH/IR stars with typical double - peaked line profile at 1667 MHz were detected. We detected thermal emission towards 51 sources, and 4 sources were observed in absorption. OH emission is supposed to be thermal when the 1665/1667 line ratio is between 1 and the LTE value of 1.8, and no polarization is present. In our sample, thermal emission sources are weaker than the masers (the maximum flux of 0.64 Jy towards 16244−2432 in ρOph cloud, in the rest of the sample flux does not exceed 0.4 Jy, the mean value being 0.19 Jy). Several sources from our list of thermal detections are difficult to classify with confidence and must be studied separately to determine whether they are masers or thermal emission sources. 03439+3233, 06587−0852, 16235−2416 and 19005−0445 may be candidate OH masers of type Ib because of their apparent dominant emission at 1667 MHz, the 1667/1665

line ratio being greater than the LTE value of 1.8. Also, 05387−0924 may be a candidate OH maser of type Ia.

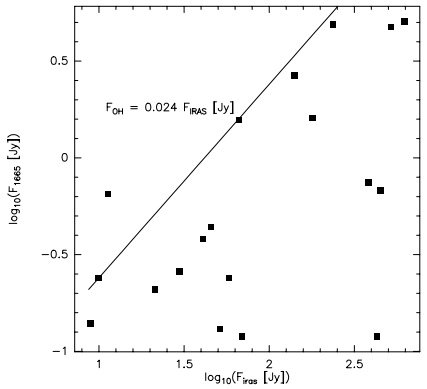

Fig. 3. A correlation between OH and IRAS fluxes. 1665 MHz fluxes of the detected masers are plotted against IRAS fluxes at 60 μm. All masers but one fall below the line $F_{\rm OH} = 0.024\ F_{\rm IR}$

The spectrum of 05487+0255 consists of two narrow components separated in velocity by approximately 3 km s^{-1}. This is probably evidence of rotation of a cloud where the line is formed.

06067+2138 shows a remarkable broad wing on the red side of the spectrum which spreads from 5 to 20 km s^{-1}. Wouterloot & Brand (1989) detected CO emission in this source at the radial velocity shifted from the maximum of the OH line by less than 1 km s^{-1}. The CO line profile also shows a red asymmetric top. This is probable evidence for a high - velocity molecular outflow both in CO and OH lines.

Finally, 36 among the 54 detected thermal sources are associated with dark nebulae from the catalogue of Lynds (1962). The estimates of OH column density made for thermal detections vary from 6.2 10^{13}cm^{-2} to 304 10^{13}cm^{-2} with a mean value of 56.7 10^{13}cm^{-2}. As the values of N(OH) range from 10^{13} to 10^{15} cm^{-2} in dark clouds (Magnani et al. 1988), our results could be considered as an evidence that the thermal OH line detected towards IRAS point sources are formed in interstellar dark clouds.

The question may arise whether the association of IRAS point sources with OH thermal emission is accidental (IRAS sources are only projected on the clouds where OH lines are forming), or real (IRAS sources are embedded in the clouds). We compared our list of thermal sources with the list of IRAS cores of Wood et al. (1994). They studied IRAS images of nearby dark clouds and identified 43 "IRAS clouds" containing 255 "IRAS cores". 15 IRAS point sources towards which we detected thermal OH lines are associated with IRAS cores of Wood et al. (1994). As the results published by Wood et al. (1994) are incomplete, this number might be greater. This means that a large fraction of the IRAS sources, towards which a thermal OH lines are detected, are really associated with the OH emitting clouds.

6. Conclusions

We have continued the survey of main line OH emission in the direction of IRAS sources, selected with Wood and Churchwell color criterion which allows to find UC HII candidates in the IRAS point sources catalog. To the observing list, we added several H_2O masers and IRAS cores. From 182 observed sources, we detected 24 certain and 5 possible OH masers, 51 thermal and 4 absorption sources. The OH flux density of the detected masers is less than 2.5 percent of infrared flux at 60 μm, which confirms the results of Cohen et al. (1988), that infrared pumping of OH masers is feasible. No new OH masers of Ib type were detected. The thermal sources that were detected are believed to be associated with nearby dark clouds. This is suggested by their low radial velocities, which in most cases coincide with that of CO lines. Also, 15 IRAS point sources have associations with IRAS cores in nearby dark clouds, identified by Wood et al. (1994). This means that IRAS point sources are connected with OH thermal emission and that the association is not only accidental.

Acknowledgements. V.I. Slysh, A.M. Dzura and I.E. Val'tts are grateful to the INSU (France), NWO (Netherlands) and Russian Foundation for Fundamental Research (grant No. 95-02-05826) for supporting this project. We thank the staff of Radioastronomy Station in Nançay for their help with observations and the referee Dr. R.J. Cohen for useful comments.

References

Benson P.J., Myers P.C., 1989, ApJS 71, 89
Blitz L., Fish M., Stark A.A., 1982, ApJS 49, 183
Casoli F., Dupraz C., Gerin M., Combes F., Boulanger F., 1986, A&A 169, 281
Cohen R.J., Baart E.E., Jonas J.L., 1988, MNRAS 231, 205
Gaylard M.J., Macleod G.C., Van der Walt D.J., 1994, MNRAS 269, 257
de Geus E.J., Bronfman L., Thaddeus P., 1990, A&A 231, 137
Heyer M.H., Snell R.L., Goldsmith P.F., Myers P.C., 1987, ApJ 321, 370
Lynds B.T., 1962, ApJS 7, 1
MacLeod G.C., 1991, MNRAS 252, 36P
Magnani L., Blitz L., Wouterloot J.G.A., 1988, ApJ 326, 909
Moore T.J.T., Cohen R.J., Mountain C.M., 1988, MNRAS 231, 887
Myers P.C., Linke R.A., Benson P.J., 1983, ApJ 264, 517
Slysh V.I., Dzura A.M., Val'tts I.E., Gerard E., 1994, A&AS 106, 87
Terebey S., Vogel S.N., Myers P.C., 1989, ApJ 340, 472
Turner B.E., 1979, A&AS 37, 1
Wood D.O.S., Churchwell E., 1989, ApJ 340, 265
Wood D.O.S., Myers P.C., Daugherty D.A., 1994, ApJS 95, 457
Wouterloot J.G.A., Brand J., 1989, A&AS 80, 149
Wouterloot J.G.A., Brand J., Henkel C., 1988, A&A 191, 323

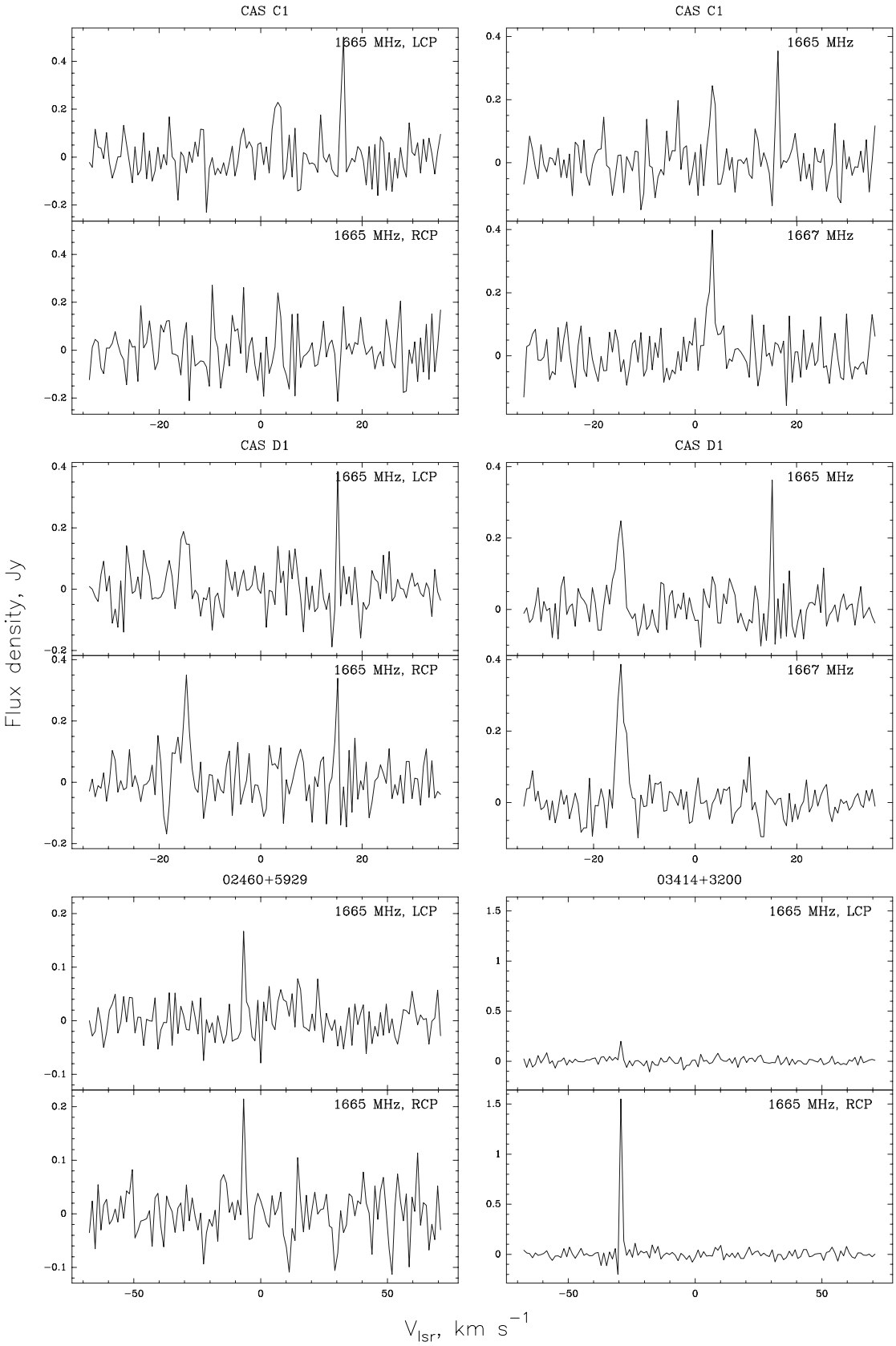

Fig. 1. 1-6). Detected masers. Frequency and polarization are marked in the upper right corner of each figure. When no polarization is specified, the spectrum is an average of the right and left hand circular polarizations

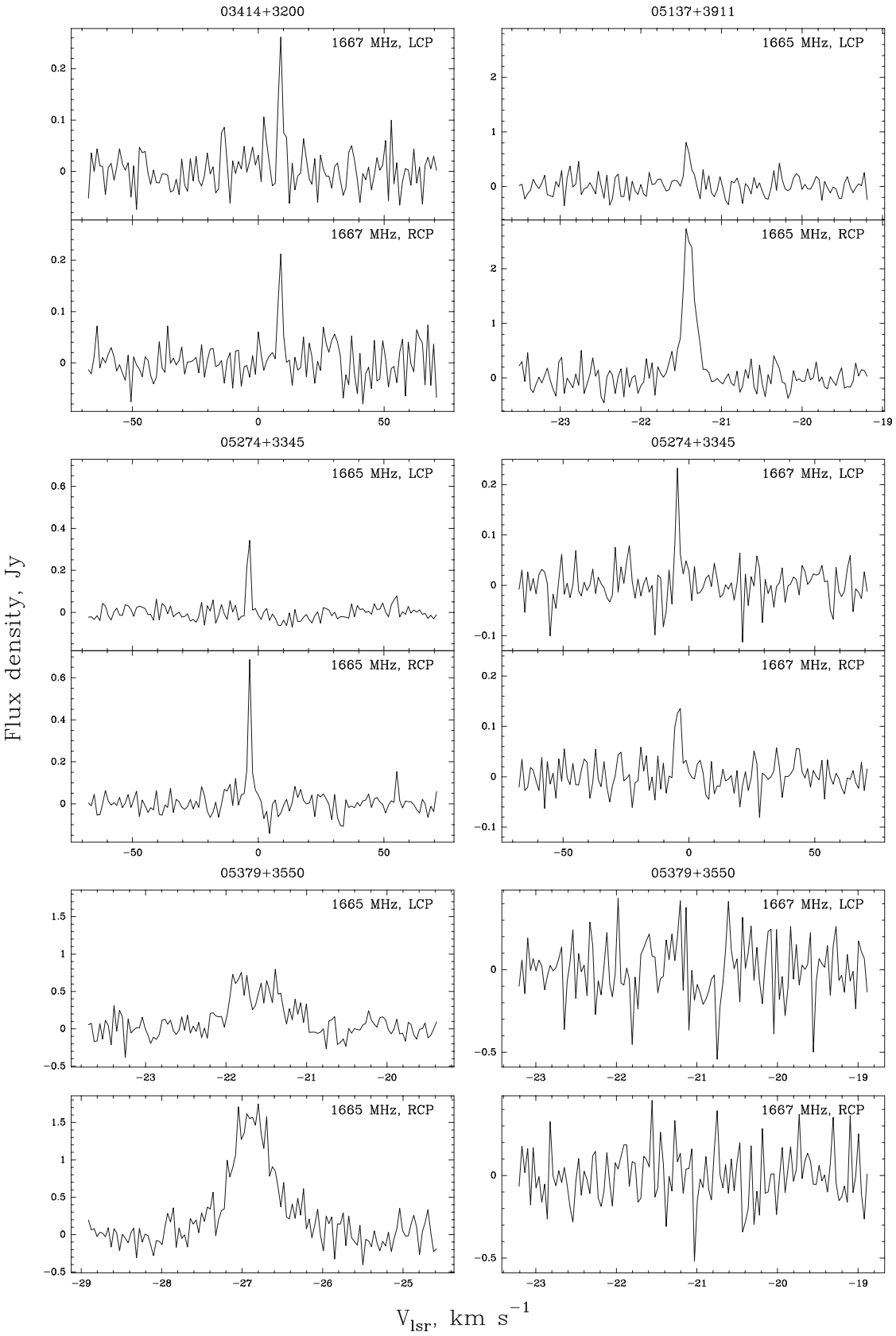

Fig. 1. 7-12). Detected masers

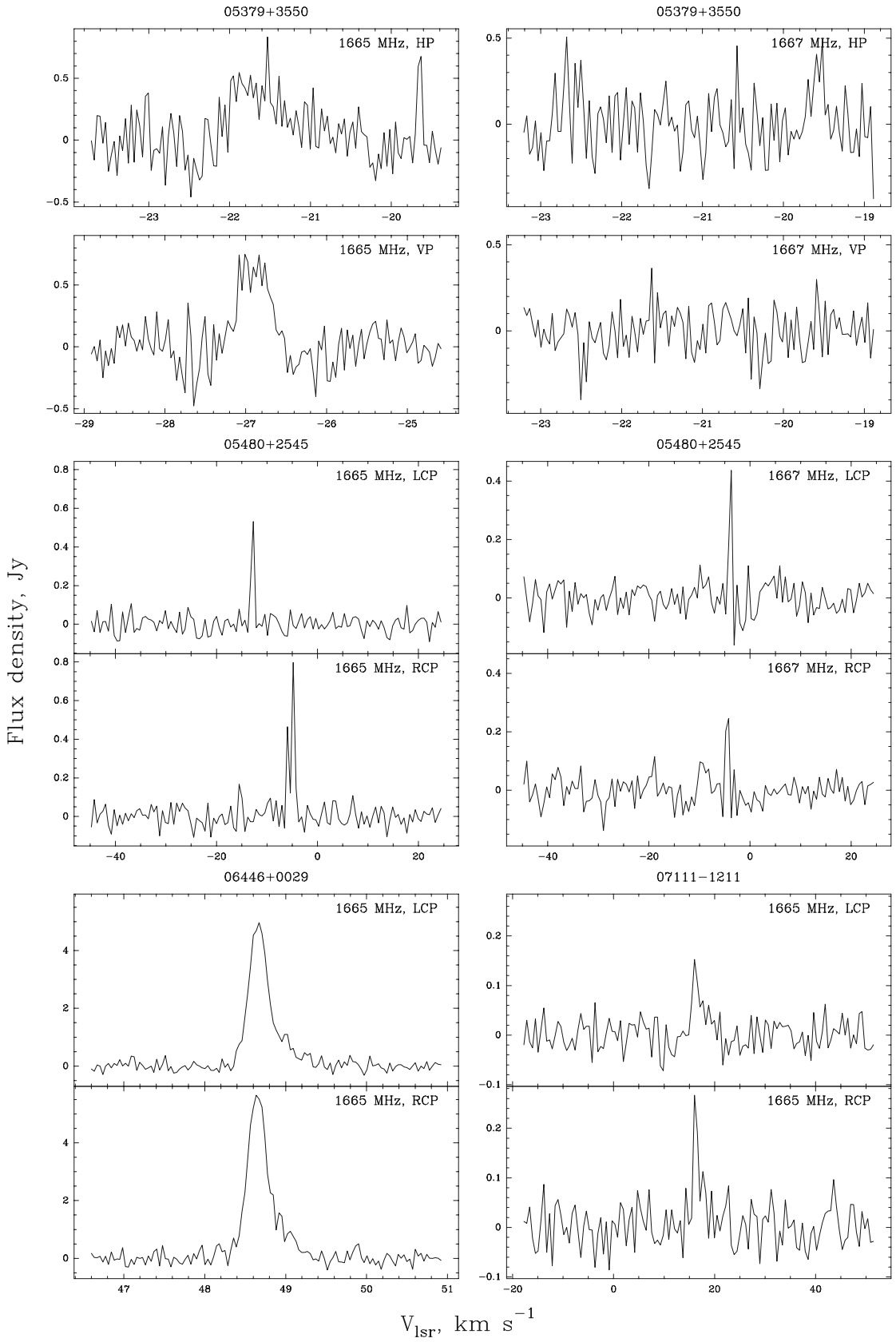

Fig. 1. 13-18). Detected masers

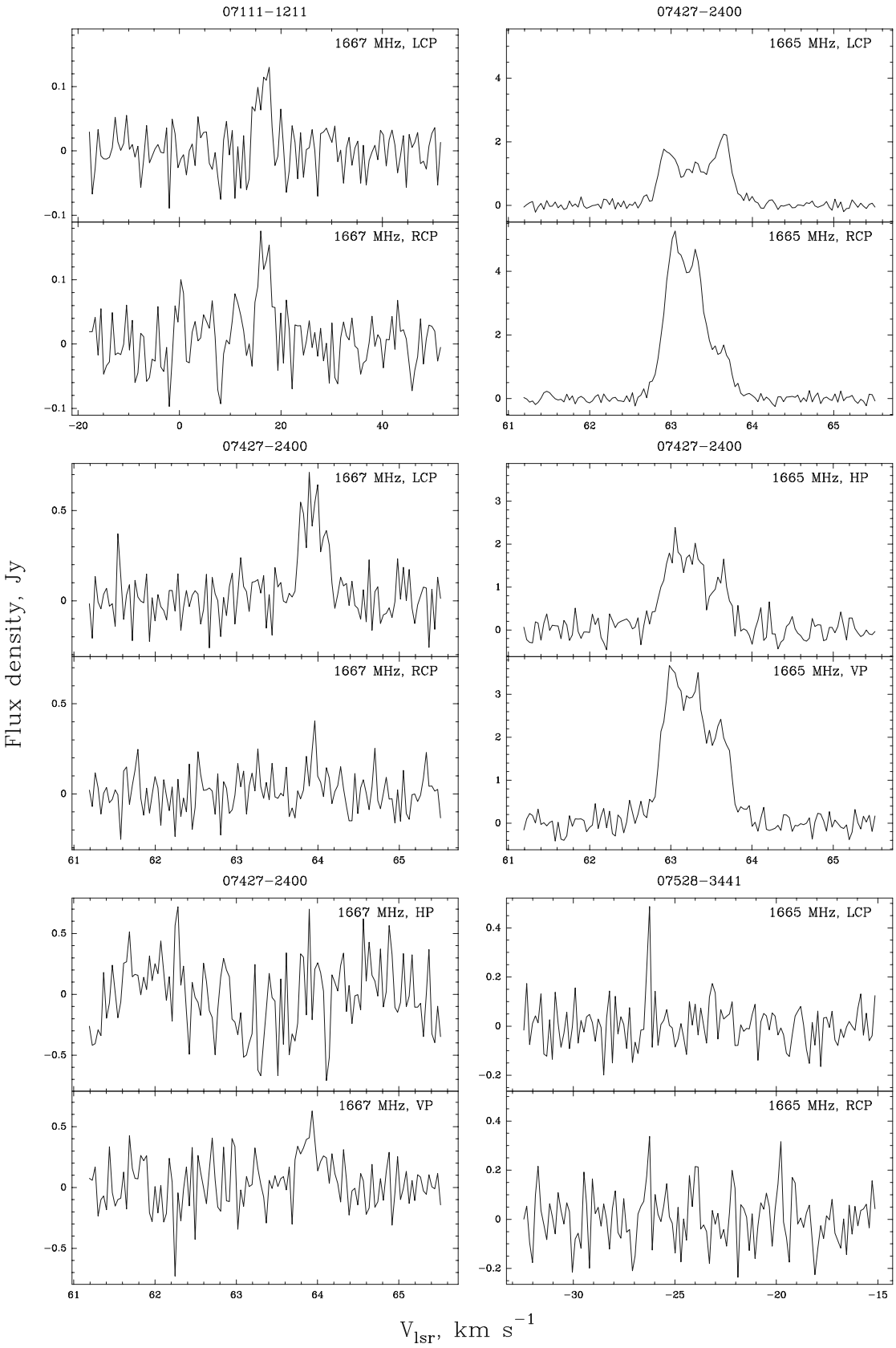

Fig. 1. 19-24). Detected masers

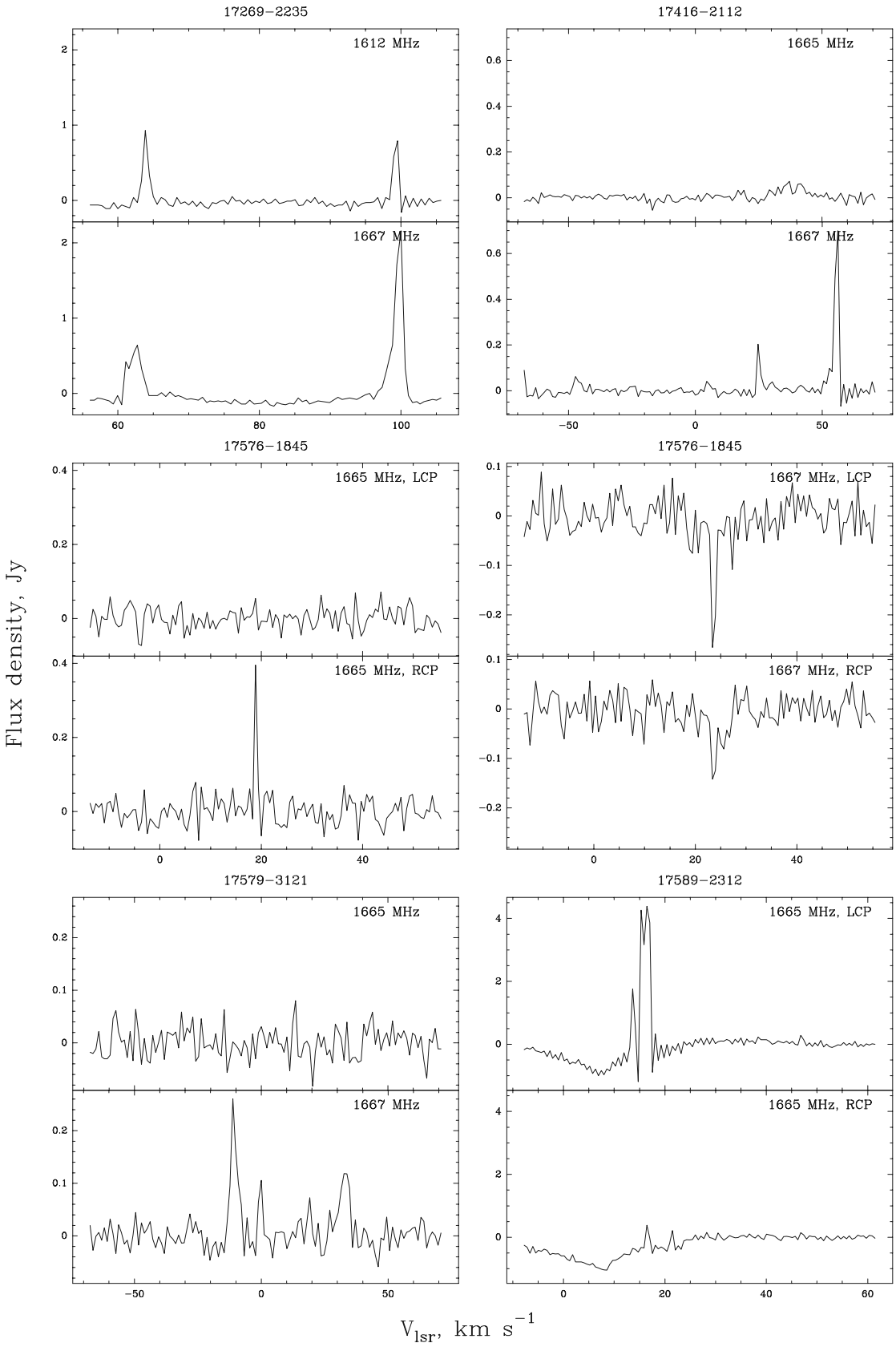

Fig. 1. 25-30). Detected masers

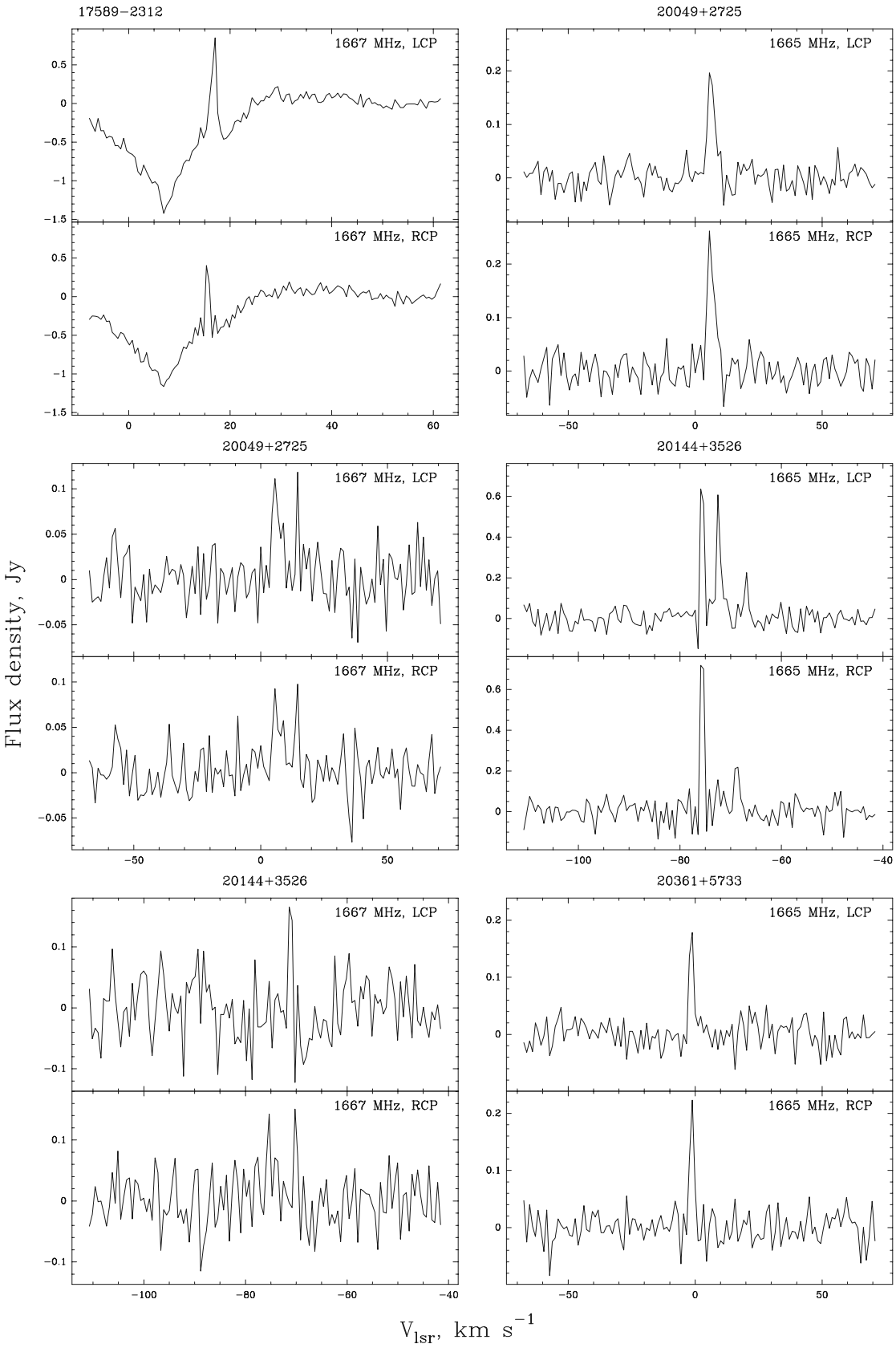

Fig. 1. 31-36). Detected masers

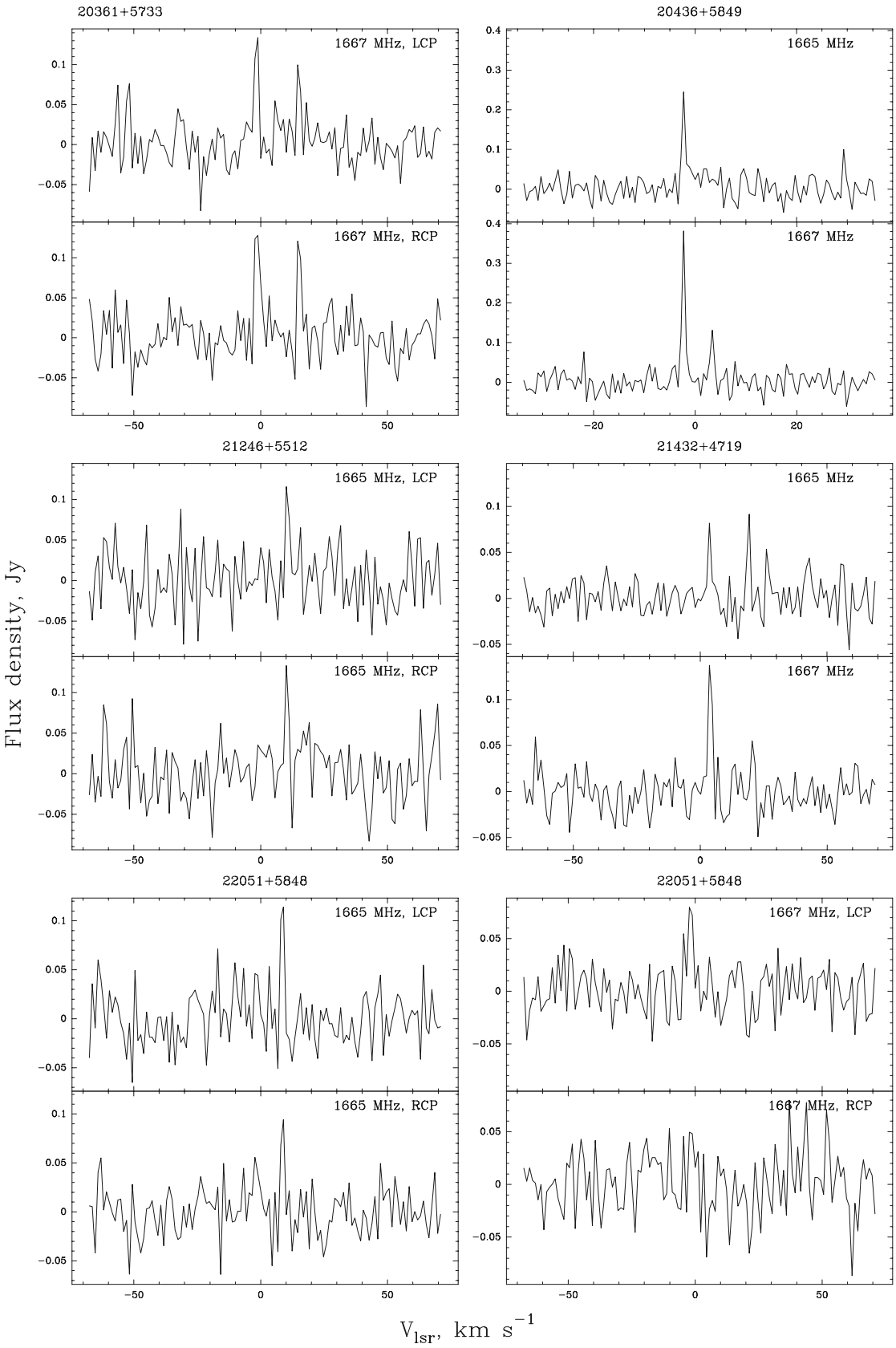

Fig. 1. 37-42). Detected masers

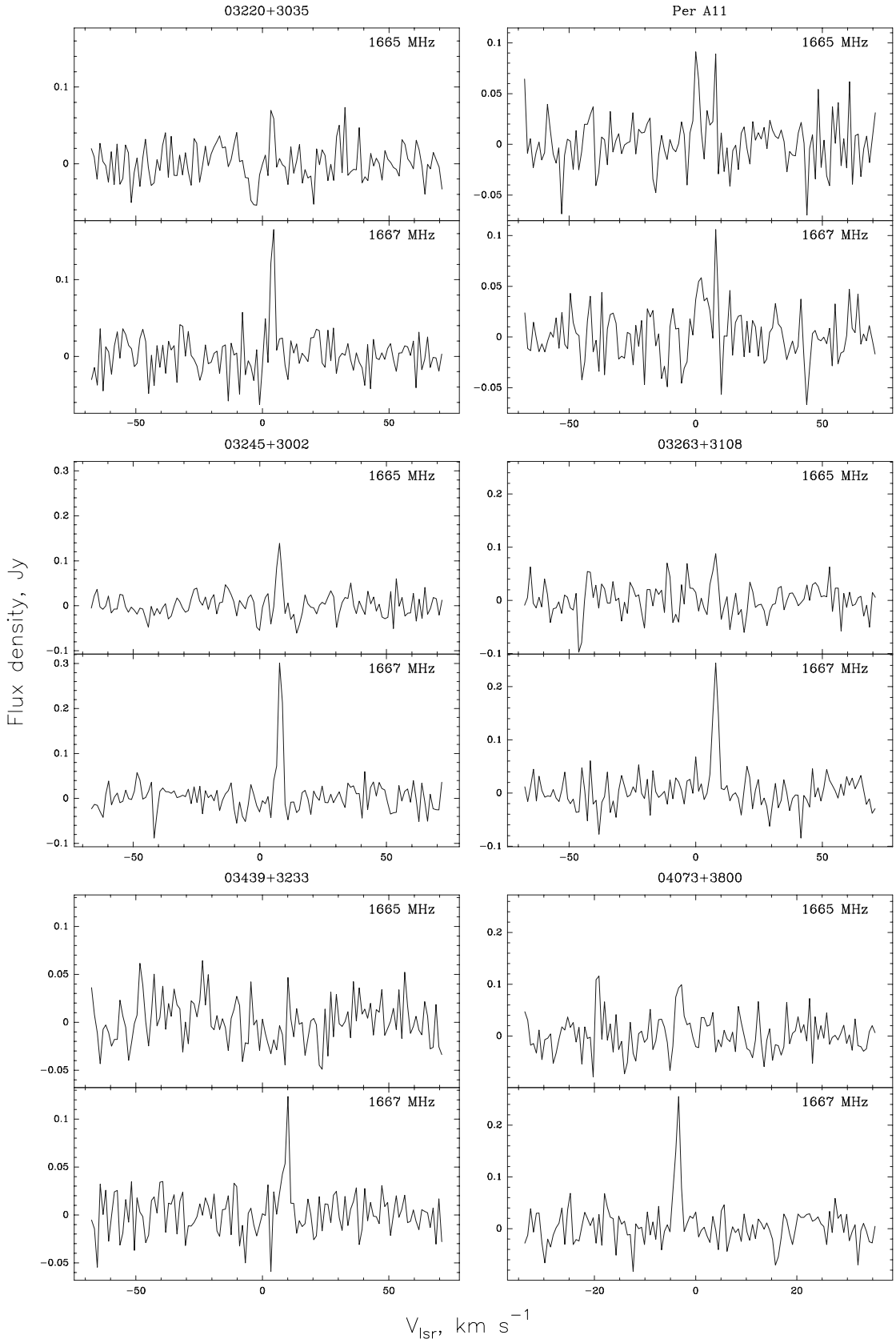

Fig. 2. 1-6). Thermal sources. Frequency is marked in the upper right corner of each figure. Spectra are averages of the right and left hand circular polarizations

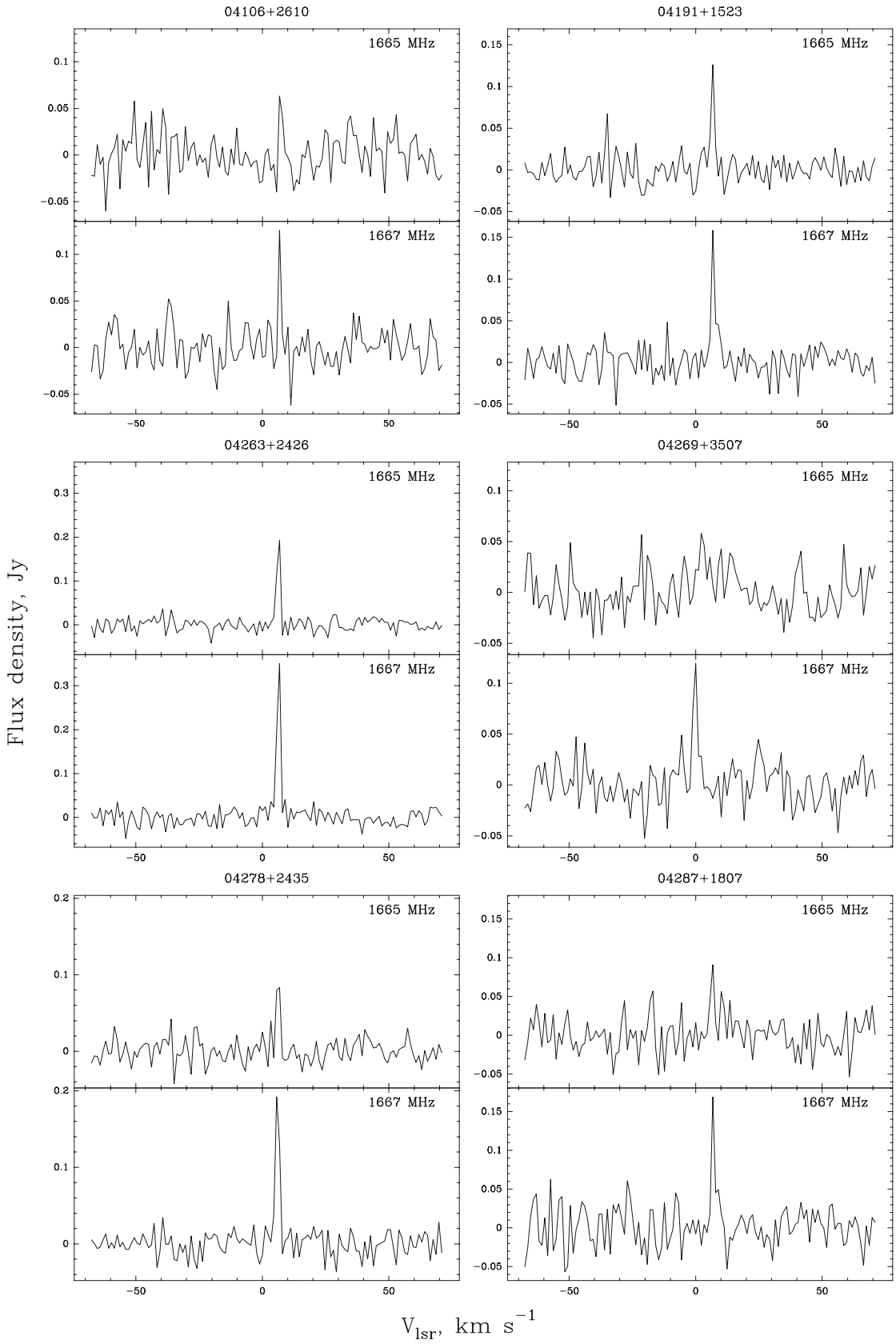

Fig. 2. 7-12). Thermal sources

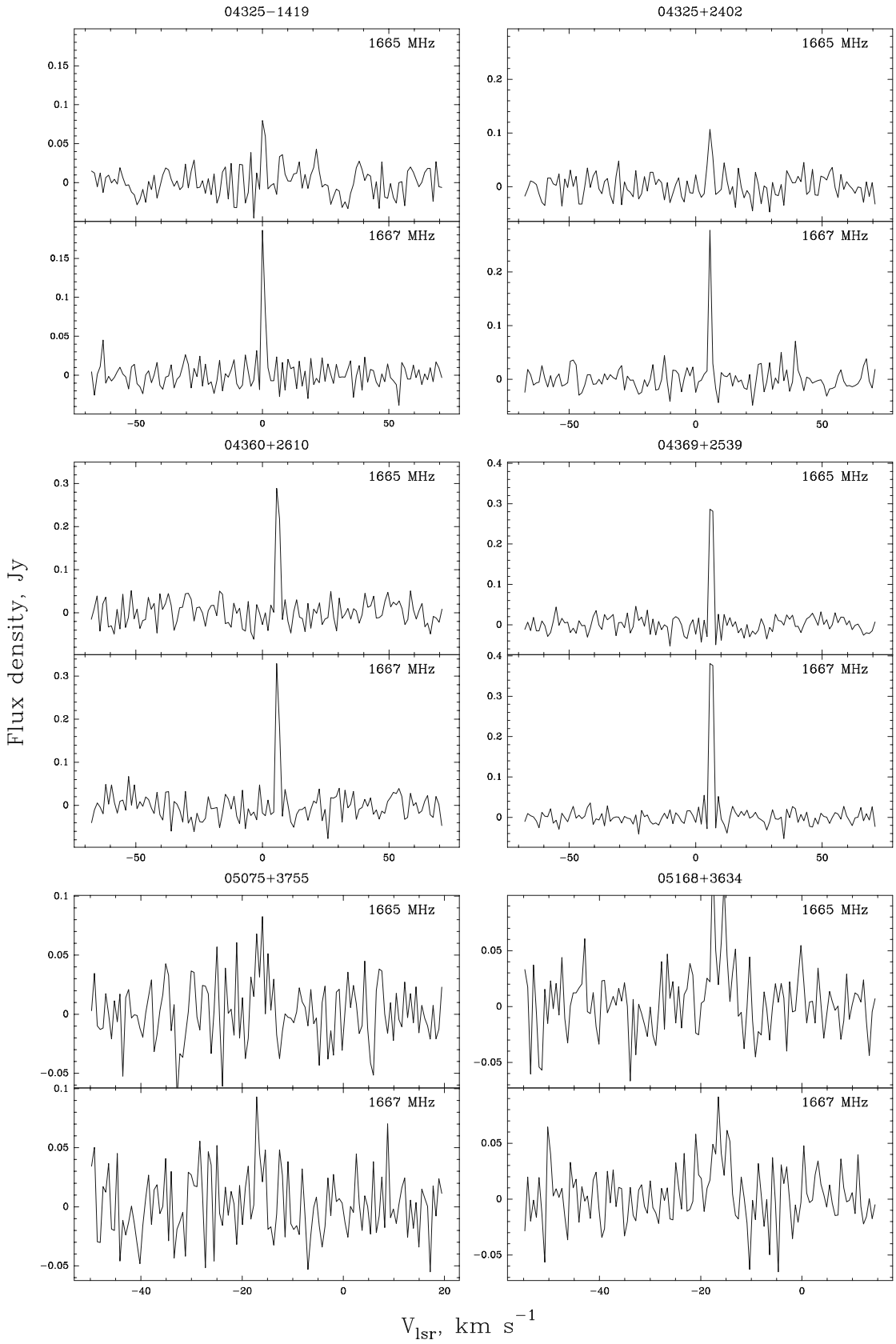

Fig. 2. 13-18). Thermal sources

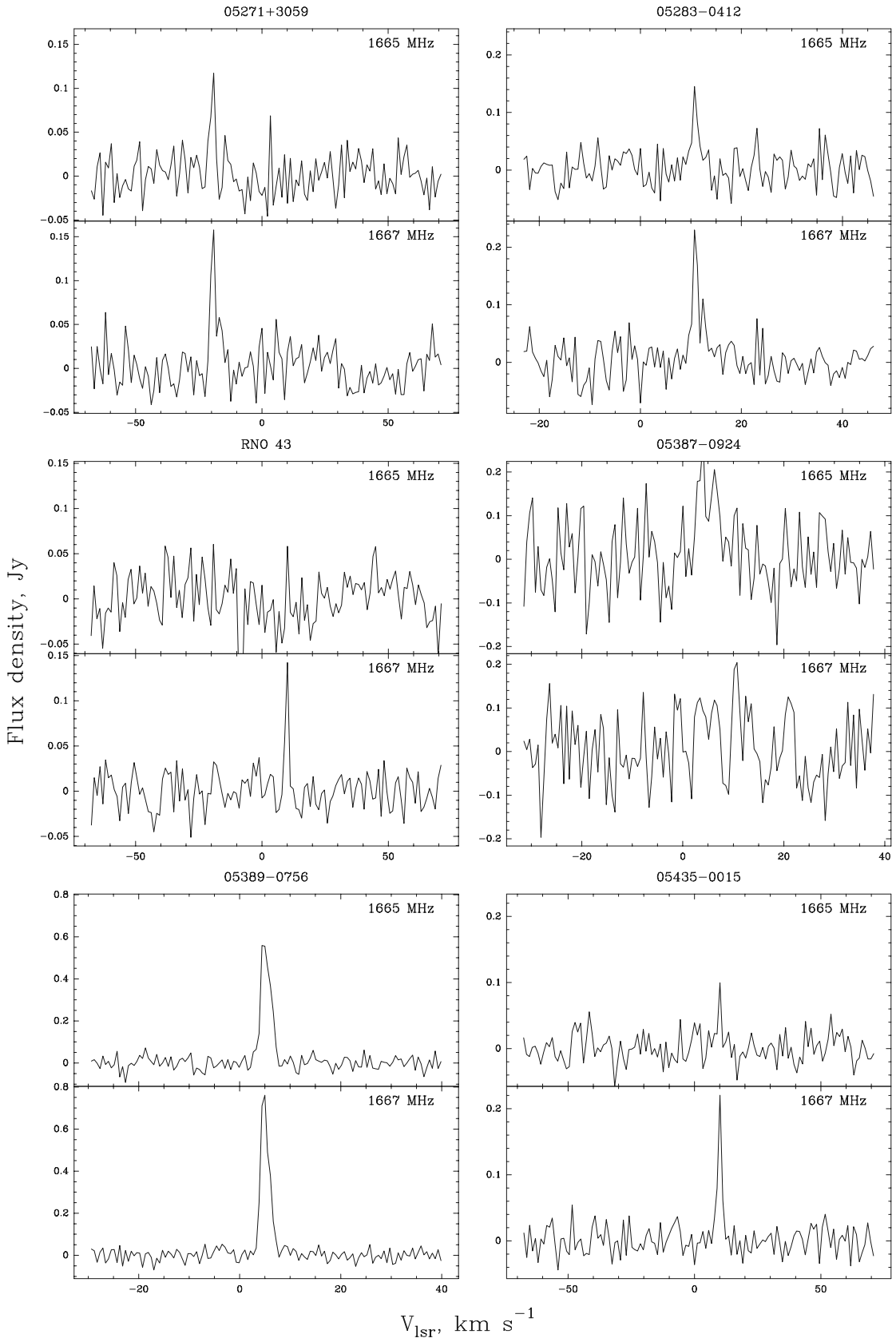

Fig. 2. 19-24). Thermal sources

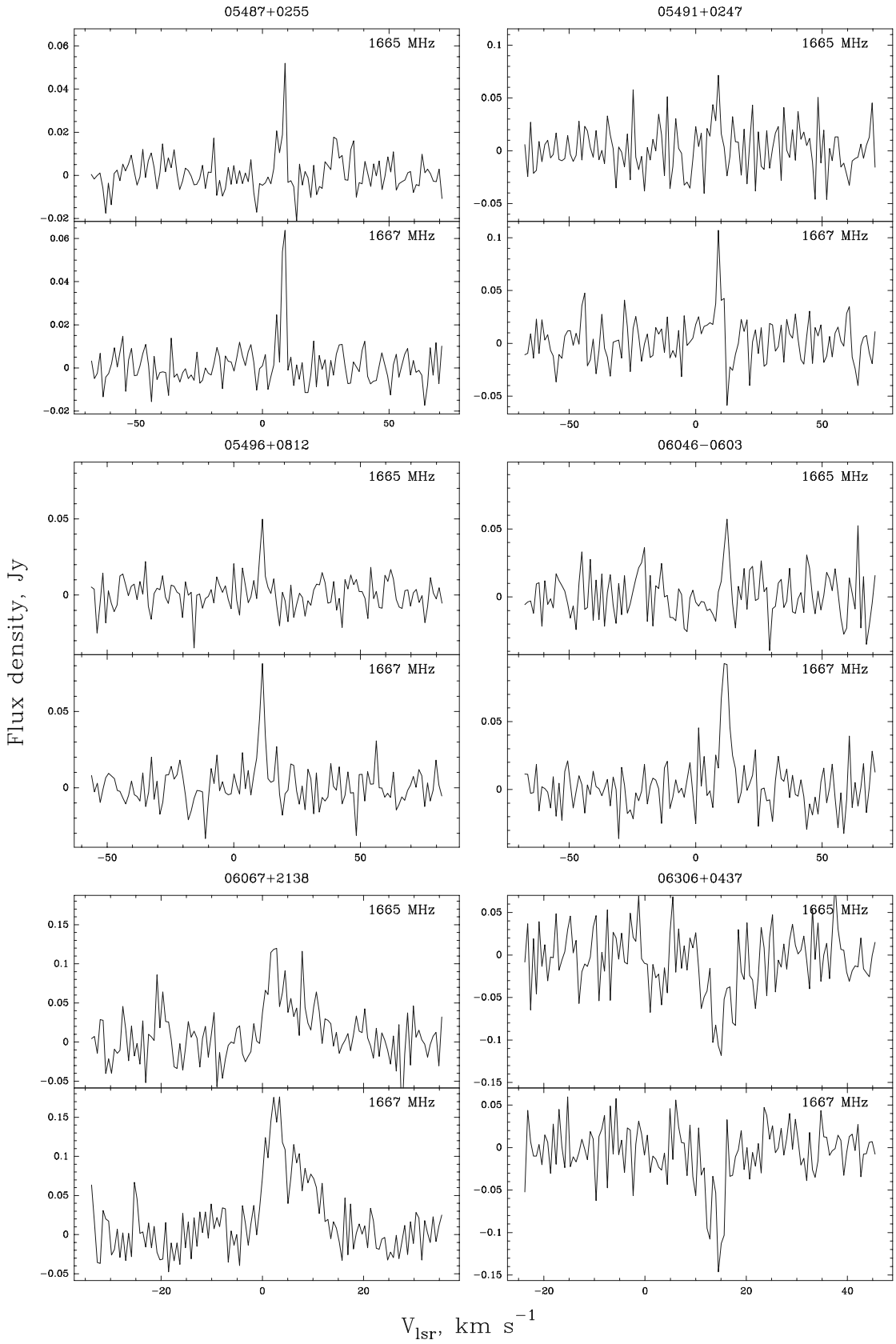

Fig. 2. 25-30). Thermal sources

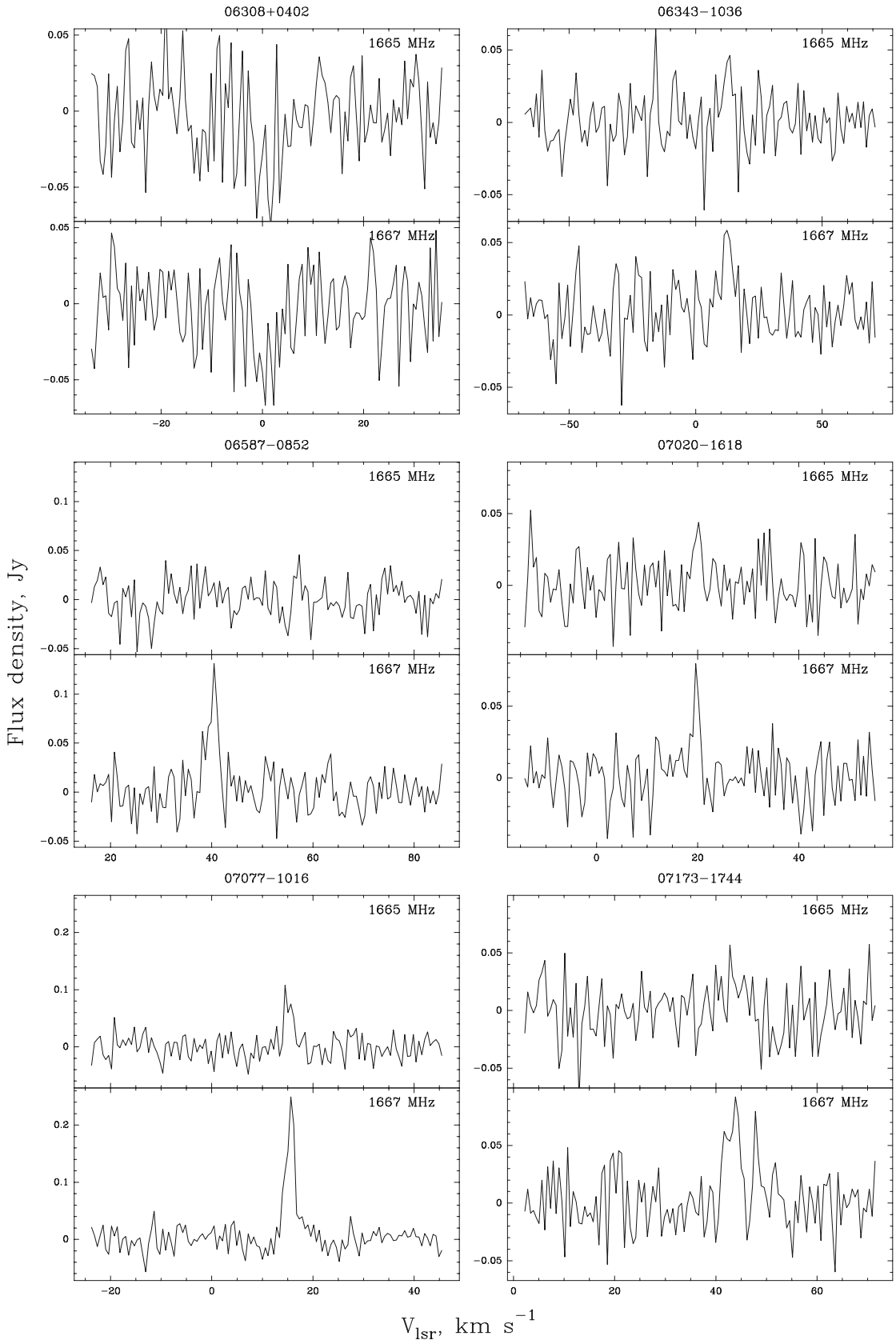

Fig. 2. 31-36). Thermal sources

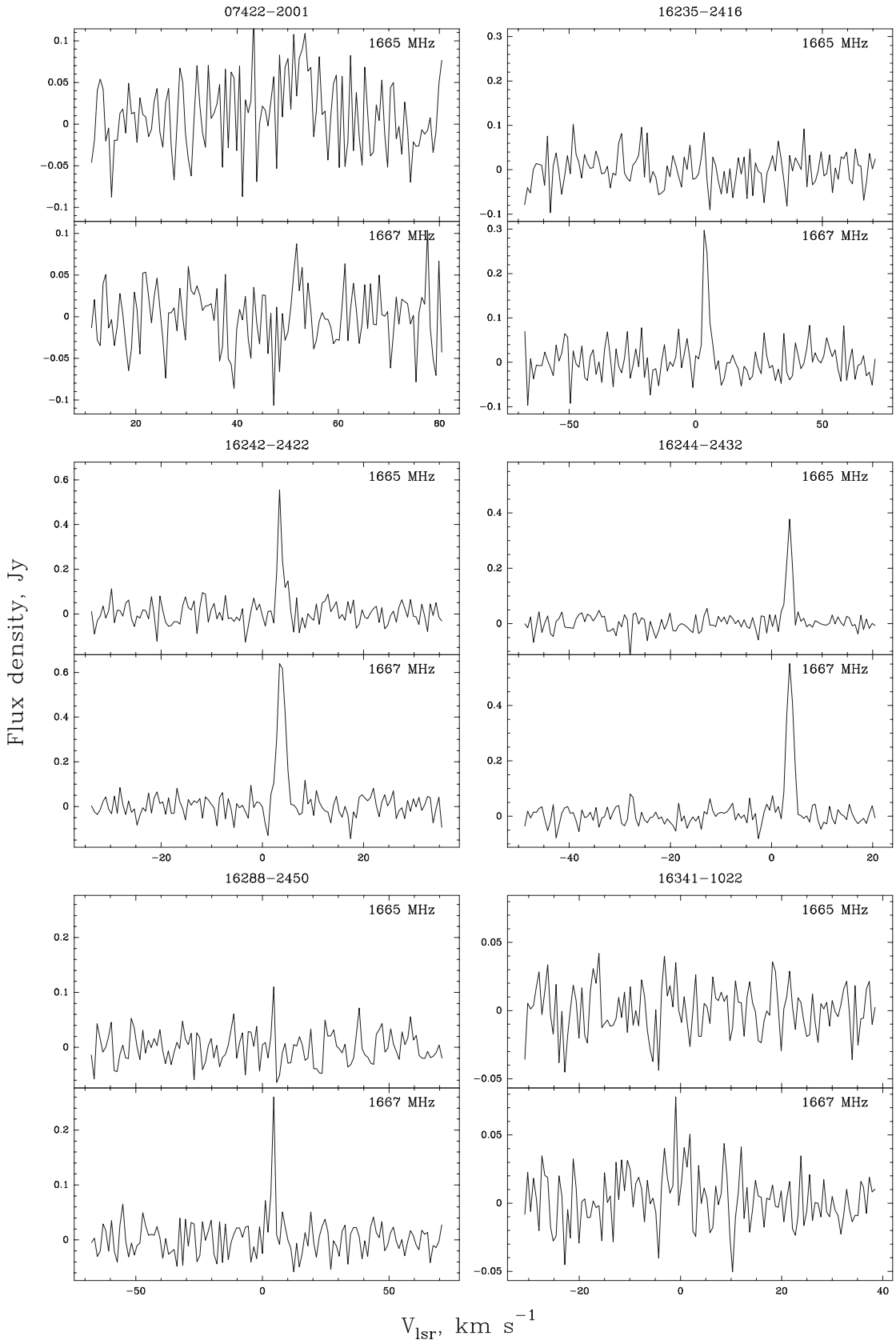

Fig. 2. 37-42). Thermal sources

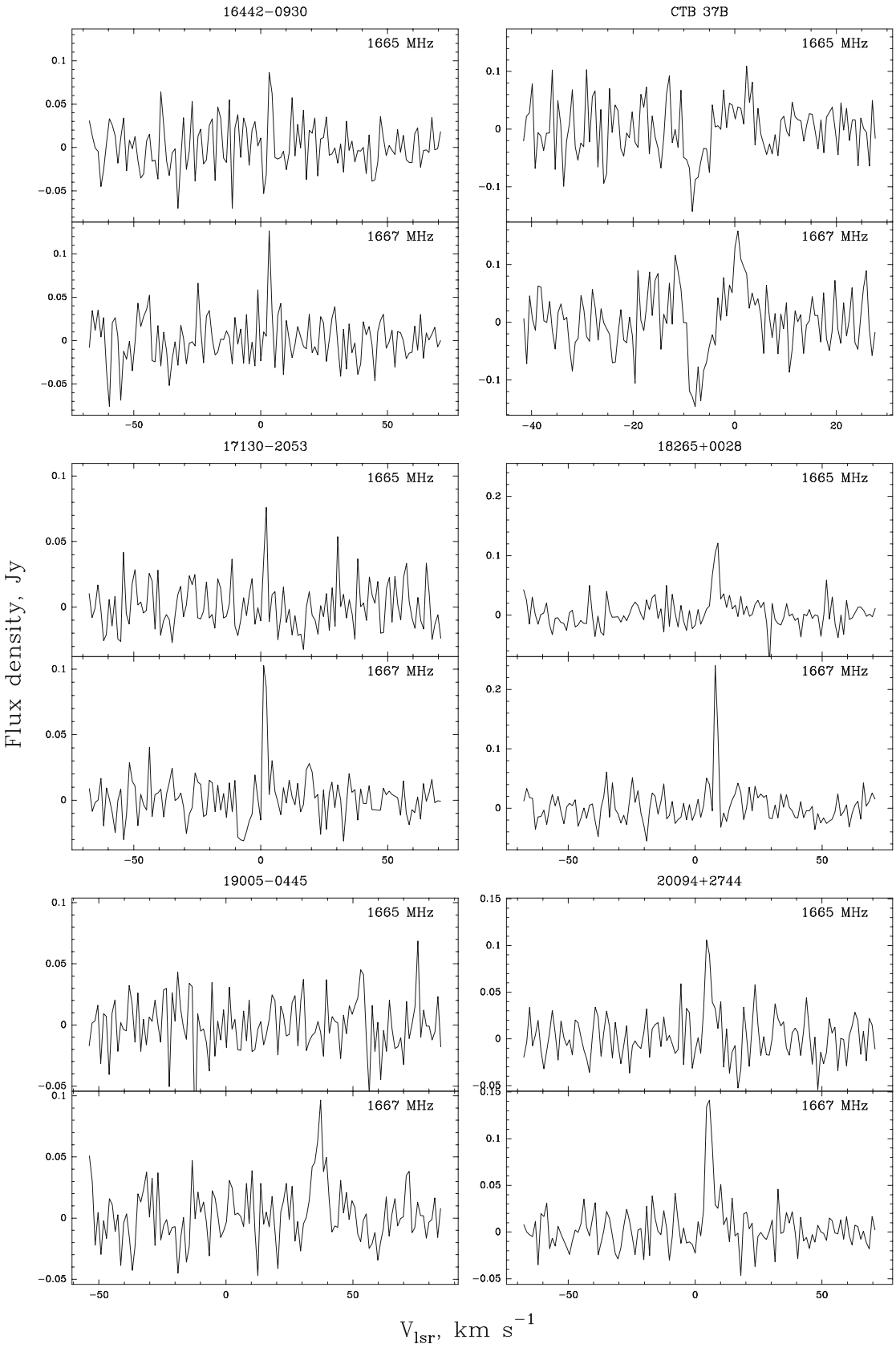

Fig. 2. 43-48). Thermal sources

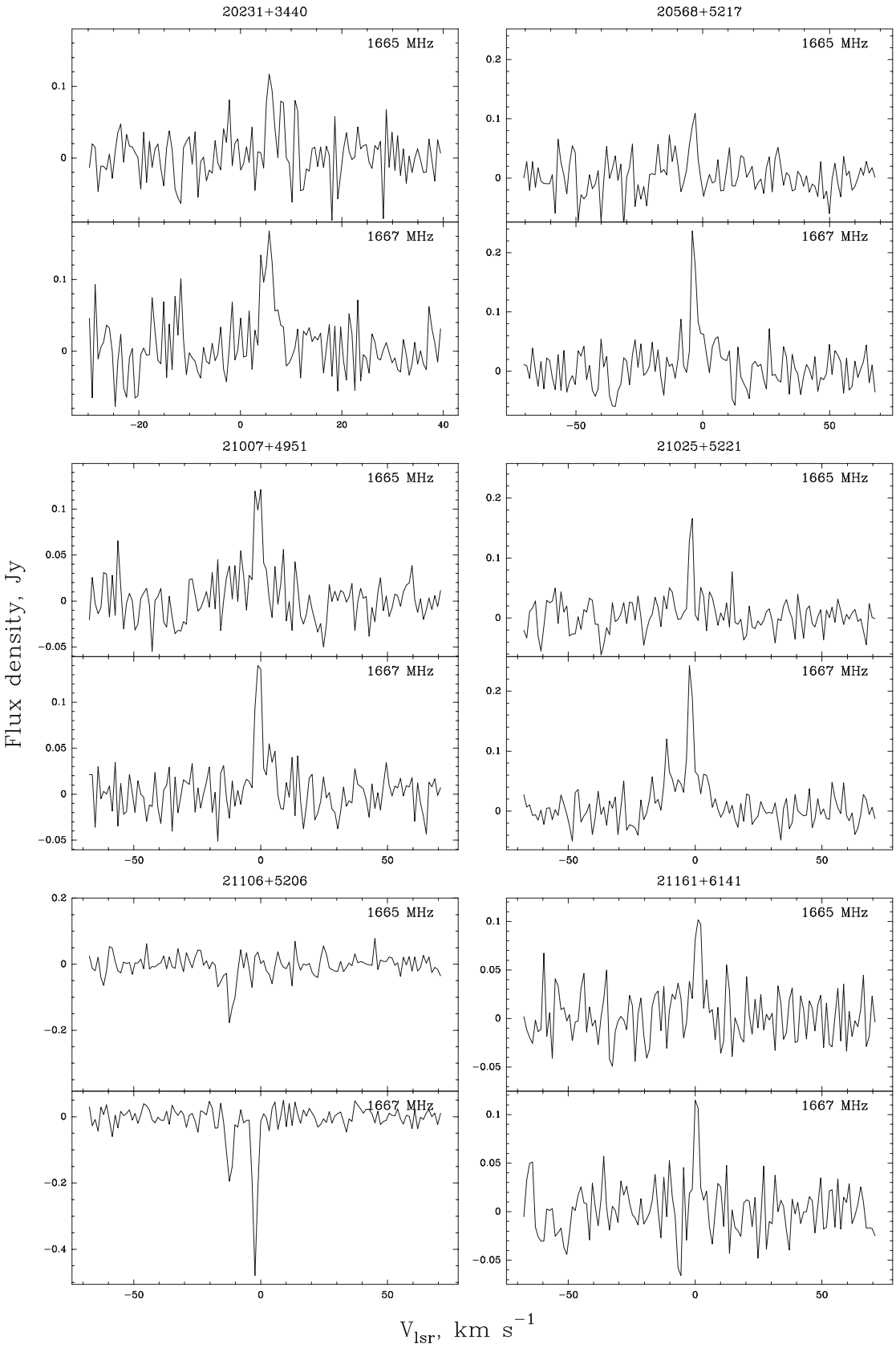

Fig. 2. 49-54). Thermal sources

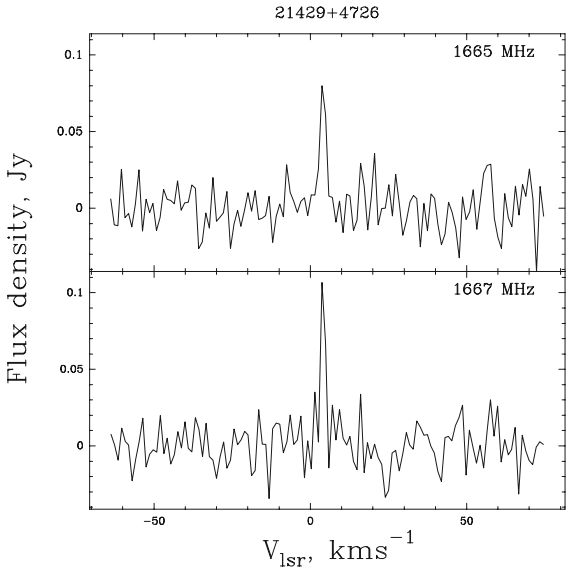

Fig. 2. 55). Thermal sources